

Topological States in Chevrel Phase Materials from First-principle Calculations

Shuai Zhang,^{1,2} Shiyu Peng,^{1,2} Xi Dai,³ and Hongming Weng^{1,2,4,*}

¹*Beijing National Laboratory for Condensed Matter Physics,
and Institute of Physics, Chinese Academy of Sciences, Beijing 100190, China*

²*University of Chinese Academy of Sciences, Beijing 100049, China*

³*Department of Physics, Hong Kong University of Science and Technology, Clear Water Bay, Hong Kong*

⁴*Songshan Lake Materials Laboratory, Dongguan, Guangdong 523808, China*

Chevrel phase materials form a family of ternary molybdenum chalcogenides with a general chemical formula $A_x\text{Mo}_6X_8$ (A = metal elements, X = chalcogen). The variety of A atoms makes a large number of family members and leads to many tunable physical properties, such as the superconductivity, thermoelectricity and the ionic conductivity. In this work, we have further found various nontrivial band topological states in these materials by using first-principle calculations. The compounds having time-reversal symmetry, such as BaMo_6S_8 , SrMo_6S_8 and Mo_6S_8 , are topological insulators in both of the $R\bar{3}$ and $P\bar{1}$ phases, whereas EuMo_6S_8 within ferromagnetic state is an axion insulator in the $R\bar{3}$ phase and a trivial one in the $P\bar{1}$ phase. This indicates that the change of A ions can modify the chemical potential, lattice distortion, and magnetic orders, which offers a unique way to influence the topological states and other properties. We hope this work can stimulate further studies of Chevrel phase materials to find more intriguing phenomena, such as topological superconducting states and Majorana modes.

INTRODUCTION

The Chevrel phase (CP) is a ternary molybdenum chalcogenides compound family [1], which was first discovered in 1971 by Chevrel and Sergent [2]. The generic chemical formula of this family is $A_x\text{Mo}_6X_8$. In its crystal structure, Mo_6X_8 can be looked as a cluster and forms a three-dimensional (3D) network. In each cluster, six Mo atoms construct an octahedron and chalcogen atoms ($X = \text{S}, \text{Se}$) form a distorted pyramid ligand field around each Mo. A fills in this cluster network with x varying from 0 to 4 [1] and it can be monovalent, divalent, trivalent or rare-earth elements. This leads to many family members and large space to tune their physical properties. Therefore, there have been lots of research done on them, and many intriguing phenomena have been found and investigated. For example, SnMo_6S_8 and PbMo_6S_8 show superconductivity at low temperature with T_c being about 14.2 and 15.2 K,

respectively [3–5]. BaMo_6S_8 and EuMo_6S_8 have been found to be superconducting under pressure around several GPa [6–10]. $\text{Ca}_x\text{Mo}_6\text{S}_8$ becomes superconducting when Ca vacancy is introduced with $x = 0.94$ [11]. Moreover, many of them have upper critical fields H_{c2} higher than 25 T and even up to 60 T [5, 8, 10], which violates the Pauli paramagnetic limit in the weak coupling Bardeen-Schrieffer-Copper superconductor [12, 13]. One of the possible reasons is the strong spin-orbit coupling (SOC) of the electrons around the Fermi level, since Mo 4d bands have been found to constitute the Fermi surface. In addition, we noticed that the resistance-temperature curve of BaMo_6S_8 shows an anomalous behavior like ZrTe_5 [14–17], which has sensitive topological phase transitions tuned by small external stimuli [18–21]. Thus, to understand these exotic physical properties, the extensive studies on their electronic structure and band topology are necessary and meaningful.

In this work, we calculated and analyzed the topological states of some sulfides in these CP materials. We have chosen four representative compounds, namely Mo_6S_8 with A site un-

* hmweng@iphy.ac.cn

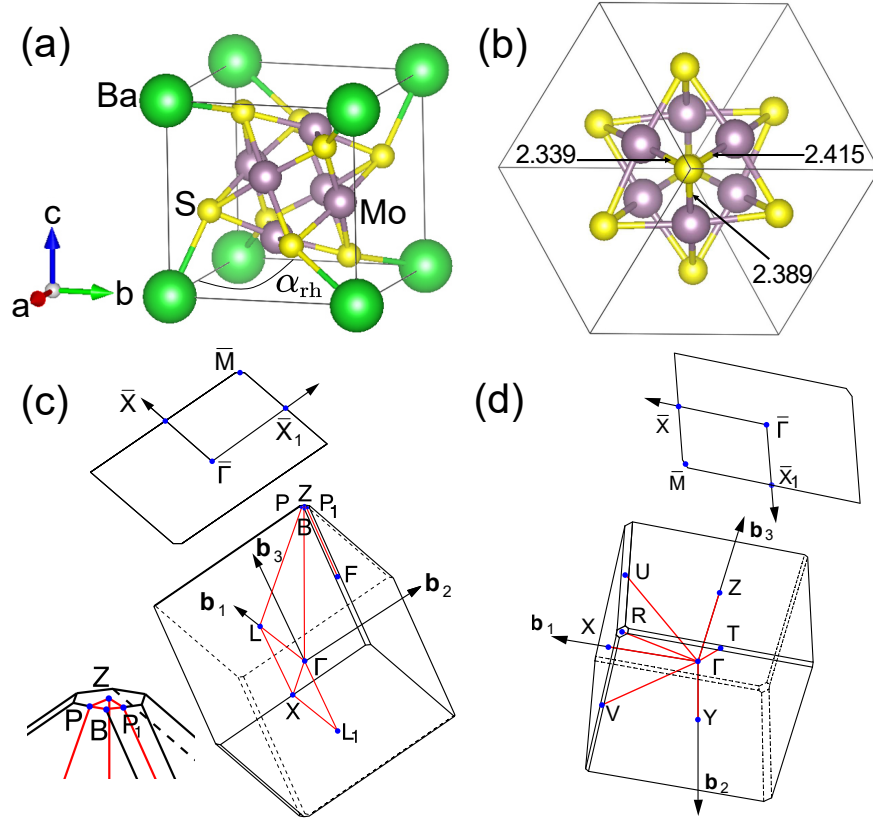


FIG. 1: Crystal structures (primitive unit cell) and Brillouin zones of BaMo_6S_8 . (a) The crystal structure of the $R\bar{3}$ phase, where the green balls represent Ba and the purple (yellow) represents Mo (S). (b) The crystal structure of the $P\bar{1}$ phase in view of $\langle 111 \rangle$ direction with Ba atoms omitted for clearness. The numbers are three Mo-S bond lengths in unit of Å. Panels (c) and (d) show the bulk and the (001) surface Brillouin zones of the $R\bar{3}$ and the $P\bar{1}$ phases, respectively. The inset in Panel (c) magnifies the part around the \bar{Z} point.

occupied, BaMo_6S_8 and SrMo_6S_8 with A site occupied by nonmagnetic divalent ions, and EuMo_6S_8 with A site occupied by magnetic rare-earth ions Eu. We found that some of them have nontrivial band topology and further studied their dependence on structural and magnetic phase transitions, as well as different occupation cases. On considering their unconventional superconductivity, the existence of nontrivial band topology will be very appealing, and their mutual coupling may induce topological superconductivity and Majorana modes,

such as those proposed in $\text{FeTe}_{1-x}\text{Se}_x$ [22, 23], the HfRuP family [24], and YCoC_2 [25].

The rest of this paper is organized as follows: First, we introduced the computational methods and software packages as well as the parameters we set. Second, we discussed the topological states of nonmagnetic compounds with BaMo_6S_8 as the representative object. Third, we studied the magnetic compound EuMo_6S_8 . Finally, we present a discussion and our conclusions.

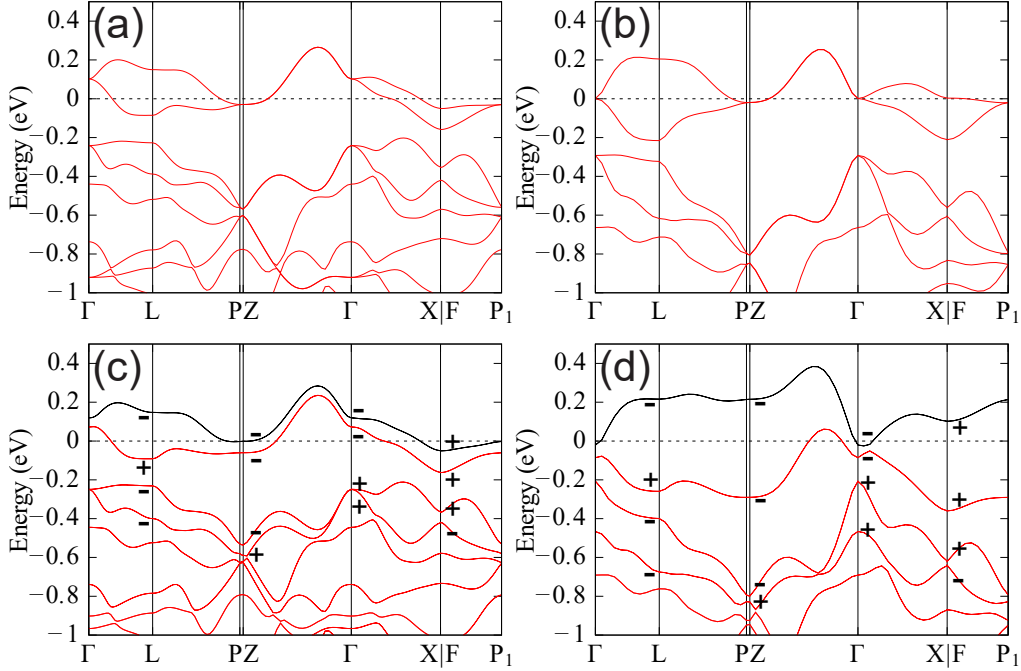


FIG. 2: The band structures of $R\bar{3}$ phase BaMo_6S_8 calculated with non-SOC PBE (a), non-SOC HSE06 (b), SOC PBE (c), and SOC HSE06 (d). In Panels (c) and (d), “-” and “+” represent the parity eigenvalues of each Kramers degenerate pair at TRIMs and the red bands are the N occupied ones, where N represents the number of valence electrons of BaMo_6S_8 . Here, the coordinates of these TRIMs are Γ (0, 0, 0), L (0.5, 0, 0), F (0.5, 0.5, 0), and Z (0.5, 0.5, 0.5).

I. METHODOLOGY

We employed the Vienna *ab initio* simulation package (VASP) [26, 27] to perform the electronic structure calculations. The projector-augmented-wave (PAW) method [28, 29] with the Perdew-Burke-Ernzerhof (PBE) exchange-correlation functional [30] was used. It is known that DFT calculation within local density approximation or generalized gradient approximation always underestimates the band gap and overestimates the band inversion. To amend this, hybrid functional HSE06 [31, 32] calculation is usually employed to check the band topology [33]. The plane-wave cutoff for kinetic energy was set as 500 eV, and a $7 \times 7 \times 7$ Γ -centered Monkhorst-Pack k -point mesh was

used to sample the Brillouin zone (BZ) in the self-consistent charge convergence calculation. To investigate the topological states, we constructed the Wannier functional based effective Hamiltonian using the WANNIER90 package [34], and performed the calculations of surface states and flow spectra of Wannier charge centers (WCCs) of occupied bands within Wilson loop scheme [35] using the WANNIERTOOLS package [36]. This package is also used when we check the existence of the in-gap node points. We constructed the Wannier functions for the bands composed of Mo d and S p orbitals.

II. RESULT AND DISCUSSION

A. BaMo_6S_8

The crystal structures and the BZs of BaMo_6S_8 are shown in Fig. 1. As most of the CP materials, it is $R\bar{3}$ phase at room temperatures and takes a structural phase transition to $P\bar{1}$ phase around 175 K [37] when temperature drops down. $R\bar{3}$ phase can be assumed as a slightly distorted cubic structure, in which the Mo_6S_8 cluster is centering the cubic lattice formed by Ba atoms. The 90° angle between the lattice vectors is reduced to 88.711° (α_{rh}) to form the $R\bar{3}$ phase [37], as shown in Fig. 1(a). The point group symmetry of $R\bar{3}$ phase is C_{3i} , where the C_3 rotation axis is along $\langle 111 \rangle$ direction in the rhombohedral lattice. As temperature drops down, the C_3 rotation symmetry is broken, and the symmetry reduces to $P\bar{1}$. This structural phase transition can be seen in the changes of the Mo-S bond lengths indicated in Fig. 1(b), where the three Mo-S bond lengths are different. The size of ions at A sites will affect the amplitude of distortion from C_3 symmetry. This distortion of Mo_6S_8 cluster is a kind of cooperative Jahn-Teller distortion [38] to form $P\bar{1}$ phase. All the crystal structures [37, 39–45] used in work are shown in the Supplementary Material [46].

Now, let us consider the electronic structures and the topological states of the $R\bar{3}$ phase. In Fig. 2, the bands around the Fermi level are mainly from Mo $4d$ orbitals and they have been proposed to be understood in the basis set composed by molecular orbitals of Mo_6 octahedral cluster [47]. In the non-SOC case, as shown in Fig. 2(a), the two bands crossing the Fermi level are two-fold degenerated along the Γ – Z path, which is protected by the C_3 rotation symmetry, and their representation is $^1E \oplus ^2E$. These two irreducible representations 1E and 2E are complex conjugate to each other. By taking the time-reversal symmetry into account, they will combine together to form a two dimensional irreducible representation of the type II magnetic group [48]. After including SOC, as shown in Fig. 2(c), the splitting in these

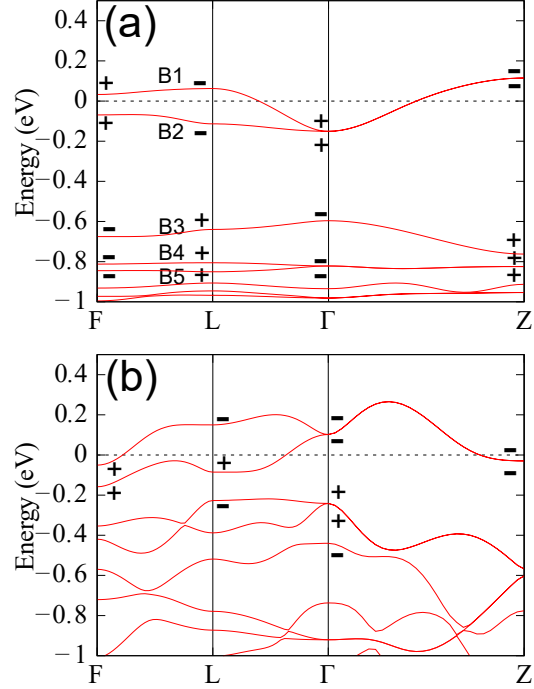


FIG. 3: (a) The non-SOC band structure calculated with scaling the lattice constants of $R\bar{3}$ phase BaMo_6S_8 by 128 % and fixing the Mo_6S_8 as a rigid cluster. “B1” “B2” and so on label each flat band. The parity eigenvalues at TRIMs are also labeled. (b) The non-SOC band structure of the real BaMo_6S_8 .

two bands is obvious, namely there are finite band gaps between these two bands (each has Kramers degeneracy) at any k point in the BZ. For this reason, SOC is necessary for getting the possible band insulator state in $R\bar{3}$ phase BaMo_6S_8 . Otherwise, it would be a filling-enforced metal [49, 50].

Now let us consider the topological states with SOC. For convenience, we denote N to represent the number of valence electrons in the case of A being a divalent ion with $x = 1$, such as BaMo_6S_8 . There are $N - 2$ valence electrons when A site is empty. When SOC is considered, the Kramers degenerated $(N - 1)$ - and N -th bands are gapped from the $(N + 1)$ - and

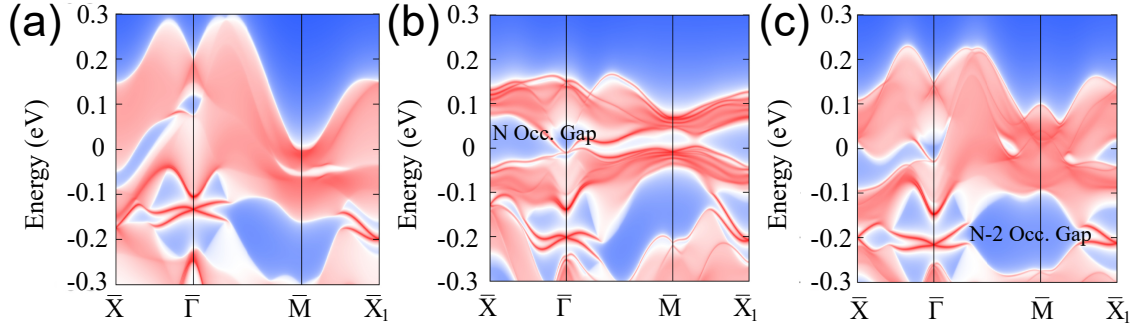


FIG. 4: The (001) surface states of $R\bar{3}$ phase BaMo_6S_8 with SOC. (a) The surface states calculated with the original band structure. (b) The surface states calculated with the renormalized band structure, which has a global gap in the N occupation case. (c) The surface states calculated with the renormalized band structure, which has a global gap in the $N - 2$ occupation case.

$(N + 2)$ -th bands at each k -point as we mentioned before. According to the Fu-Kane formula [51], we can get the topological \mathbb{Z}_2 indices $(v_0; v_1, v_2, v_3)$ from the parity eigenvalues of all occupied Kramers degenerate pairs on time-reversal invariant momenta (TRIMs).

We found if all the lowest $N + 2$ bands were occupied, the \mathbb{Z}_2 indices are $(0; 0, 0, 0)$. If all the lowest N bands are occupied (i.e., the N occupation case), the \mathbb{Z}_2 indices are $(1; 0, 0, 0)$, which means the \mathbb{Z}_2 indices for Kramers degenerated $(N + 1)$ - and $(N + 2)$ -th bands are $(1; 0, 0, 0)$. If all the lowest $N - 2$ bands are occupied (i.e., the $N - 2$ occupation case, namely A is unoccupied), the \mathbb{Z}_2 indices are $(1; 1, 1, 1)$, which means the \mathbb{Z}_2 indices for the $(N - 1)$ - and (N) -th bands are $(0; 1, 1, 1)$. From these \mathbb{Z}_2 indices, the gap between the group of the lowest $N - 2$ bands and that of $N - 1$ to $N + 2$ bands is topologically non-trivial. That means there is band inversion happening between these two groups, which indicates there must be nodal line(s) in this gap in the non-SOC case [52]. The detailed calculations including the parity distribution and WCCs are shown in the Supplementary Material [46].

The band structures with HSE06 functional are shown in Figs. 2(b) and 2(d). In the non-SOC + HSE06 case, the band structure is much

more like a semimetal than the PBE case. But the degeneracy of the bands crossing the Fermi level along the Γ -Z path remains. In the SOC + HSE06 case, such degeneracy is broken, and the band gap between them is much more enlarged than PBE case with small electron and hole pockets left. Comparing the parities in both cases, the parity eigenvalues and their distribution of the N -th and the $(N + 2)$ -th bands are not changed as shown in Figs. 2(c) and 2(d). So the topological states from HSE06 functional are not changed.

For a better understanding of the topological states in both the $N - 2$ occupation and the N occupation cases, we investigated the band inversion mechanism, which provides an intuitive picture of topological phase transitions. Let us consider the non-SOC condition first. By scaling the lattice vectors by 128 % and fixing the Mo_6S_8 cluster as a rigid molecular centering on the $(0.5, 0.5, 0.5)$ inversion center, the hopping between the clusters have been reduced and we got topologically trivial flat bands as shown in Fig. 3(a). We labeled the flat bands as “B1,” “B2,” and so on. B1 and B2 can be represented as the elementary band representation (eBR) $^1E_g^2E_g@3b$. B3 is from eBR $A_u@3b$, and B4 and B5 are from eBR $^1E_u^2E_u@3b$.

To clarify the topological states in both the

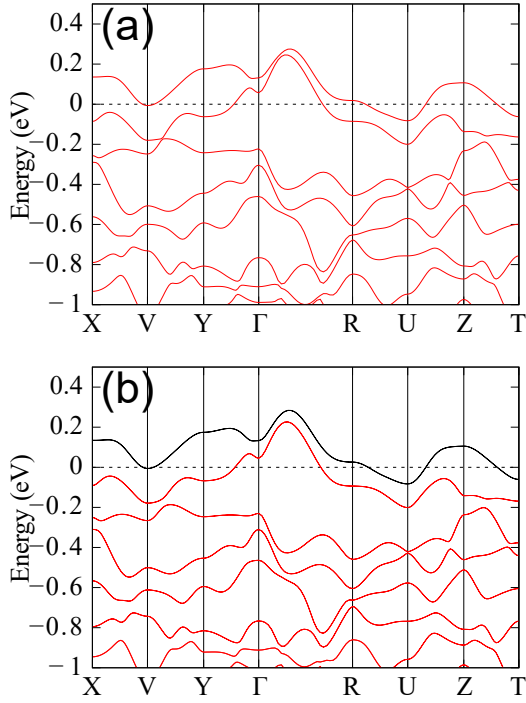


FIG. 5: The band structures of $P\bar{1}$ phase BaMo_6S_8 without SOC (a) and with SOC (b). In panel (b), the red bands are the N occupied bands, where N represents the number of valence electrons of BaMo_6S_8 .

N occupation and the $N - 2$ occupation cases, we only need to tell which bands (i.e., B3, B4, and B5) inverted with the B1 and B2 in the real crystal because the other lower bands are not entangled with B1 and B2 until the lattice constants reduce to the real values. Comparing the parity eigenvalues at TRIMs (i.e., Γ , Z, L and F points) in the flat bands and those in the real crystal, we can find the following:

- 1) At the Γ point, B1, B2 (with “+” parity eigenvalues) and B4, B5 (with “-” parity eigenvalues) are inverted;
- 2) At the L point, the parities of B1 and B2 change from two negative values to one negative and one positive, which means there is band inversion happens. Comparing Figs. 2(c)

and 3(b), we can find that SOC can only lift the band degeneracy but not affect the parity distribution at TRIMs. The hopping between the molecular orbitals from Mo_6S_8 clusters is crucial to the band inversion.

We further calculated the (001) (rhombohedral basis) surface states of $R\bar{3}$ phase BaMo_6S_8 with SOC as shown in Fig. 4(a). Because of the absence of global gap in both N and $N - 2$ occupation cases, the surface Dirac cone is mixed with the bulk states. Therefore, we artificially shifted all the *ab initio* bands at every k point by a k -dependent energy value, which does not change the energy order of the bands and the band topology, but it results in a global band gap. The details of this method are described in the Supplementary Material [46]. For later convenience, we call this procedure “renormalization”. We constructed two renormalized band structures which have global gap in the N and $N - 2$ occupation cases, respectively. Based on these renormalized band structures, we calculated the corresponding surface states with 0.02 and 0.01 eV onsite energy correction to the atoms in the surface region for the N occupation and $N - 2$ occupation cases, respectively. As shown in Figs. 4(b) and 4(c), there is a global gap in bulk states and clear surface Dirac cones in both cases. In the N occupation case, there is only one surface Dirac cone at $\bar{\Gamma}$ and there are three surface Dirac cones in $N - 2$ occupation case at \bar{X} , $\bar{\Gamma}$ and \bar{X}_1 . The number and the distribution of surface Dirac cones are consistent with the parity distribution.

Now let us consider $P\bar{1}$ phase BaMo_6S_8 . The electronic structure of $P\bar{1}$ is quite similar to the $R\bar{3}$ phase. The obvious difference is that there is no double degenerated band in the non-SOC case due to the breaking of C_3 rotation symmetry, as shown in Fig. 5(a). With the inversion symmetry retained, we can still get their topological states from Fu-Kane formula. Due to the tiny difference in both the crystal and electronic structures between $R\bar{3}$ and $P\bar{1}$ phases, the topological \mathbb{Z}_2 indices remain unchanged in both of the $N - 2$ occupation and N occupation cases. The detailed information (including the parity distribution, WCCs, and surface states)

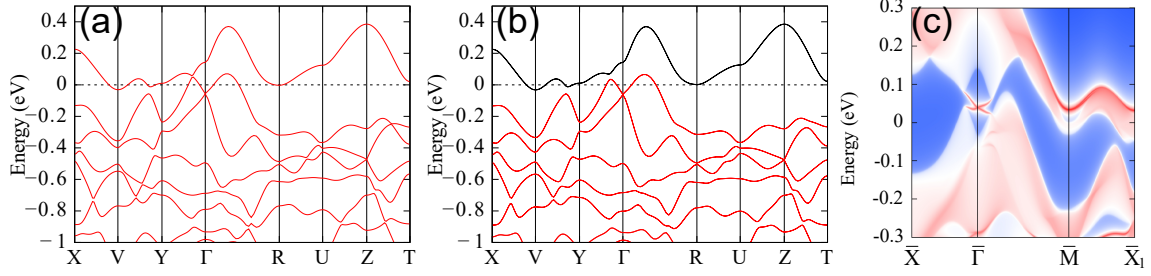


FIG. 6: The band structures without SOC (a) and with SOC (b) of $P\bar{1}$ phase SrMo_6S_8 . In panel (b), the red bands are the N occupied ones, where N represents the number of the valence electrons of BaMo_6S_8 . (c) The (001) surface states of $P\bar{1}$ phase SrMo_6S_8 with SOC.

is shown in the Supplementary Material [46].

B. SrMo_6S_8 and Mo_6S_8

In the $R\bar{3}$ phase, the crystal structure and the band structure of SrMo_6S_8 are basically the same as $R\bar{3}$ phase BaMo_6S_8 , except for the larger bandwidth of SrMo_6S_8 due to the smaller lattice constants. The topological \mathbb{Z}_2 indices of $R\bar{3}$ phase SrMo_6S_8 are the same as $R\bar{3}$ phase BaMo_6S_8 in both of the $N - 2$ occupation and the N occupation cases. We do not repeat the discussion in the main text. The band structures and the information of the topological states of $R\bar{3}$ phase SrMo_6S_8 are shown in the Supplementary Material [46].

As shown in Figs. 6(a) and 6(b) for $P\bar{1}$ phase SrMo_6S_8 , the gap between the N - and the $(N + 2)$ -th bands at Γ point is much larger than the one in $P\bar{1}$ phase BaMo_6S_8 , and there are only small electron- and hole- pockets near the Fermi level. This may be attributed to the subtle difference between the structures of BaMo_6S_8 and SrMo_6S_8 in the $P\bar{1}$ phase, as shown in the Supplementary Material [46].

In the N occupation case, the topological \mathbb{Z}_2 indices with SOC are $(1; 0, 0, 0)$, which are the same as $P\bar{1}$ phase BaMo_6S_8 . The larger bulk band gap at Γ leads to a clear surface Dirac cone as shown in Fig. 6(c), which is calculated normally without above renormalization procedure. But for the $N - 2$ occupa-

tion case, the topological \mathbb{Z}_2 indices with SOC are $(0; 1, 1, 1)$. They are different from those of $P\bar{1}$ phase BaMo_6S_8 . The nearly closing band gap at the Γ point indicates SrMo_6S_8 is close to the topological phase transition point from $(1; 1, 1, 1)$ to $(0; 1, 1, 1)$ due to the crystal distortion induced by replacing Ba with smaller Sr ions.

Because the topological state of BaMo_6S_8 in the $N - 2$ occupation case is a strong topological insulator, it is natural to reduce two valence electrons by removing the divalent metal atoms (i.e., Ba) to get a topological insulator with a large gap near the Fermi level. This is exactly Mo_6S_8 with the A site empty. In the $R\bar{3}$ phase, Mo_6S_8 has a similar crystal structure to that of BaMo_6S_8 . The lattice constant is 6.428 \AA and α_{rh} is large then 90° (i.e., 91.250°) [41, 42]. Thus, the Brillouin zone is different from BaMo_6S_8 which have divalent metal atoms. The crystal structure and the Brillouin zone of $R\bar{3}$ phase Mo_6S_8 are shown in Fig. 7.

But from the band structures shown in Fig. 8, the gap is not as large as we expected before. The \mathbb{Z}_2 indices with SOC are $(1; 1, 1, 1)$, which are the same as those of BaMo_6S_8 in the $N - 2$ occupation case. The detailed information can be found in the Supplementary Material [46].

For the $P\bar{1}$ phase, Mo_6S_8 has quite different crystal structure from BaMo_6S_8 and SrMo_6S_8 and the electronic structure is also quite different from them, as shown in Fig. 9. The \mathbb{Z}_2 indices with SOC are $(1; 0, 0, 1)$, which are dif-

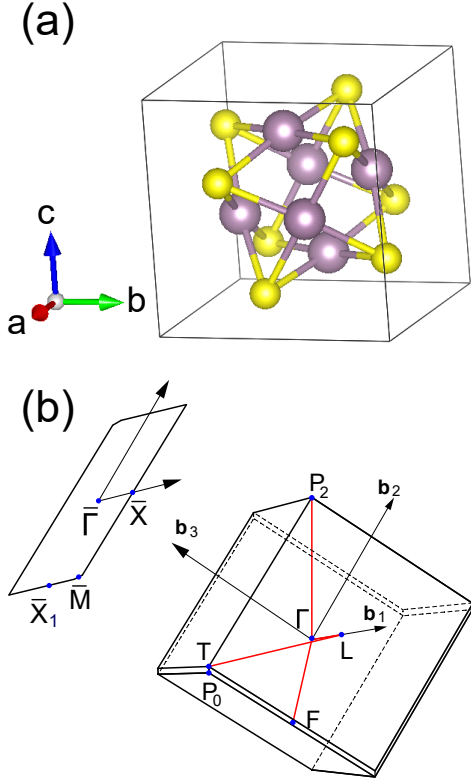


FIG. 7: Crystal structure (a) and Brillouin zone (b) of $R\bar{3}$ phase Mo_6S_8 . The purple atoms and yellow atoms represent Mo and S, respectively.

ferent from BaMo_6S_8 and SrMo_6S_8 in the $P\bar{1}$ phase and the $N - 2$ occupation case. The parity distribution is shown in the Supplementary Material [46].

C. EuMo_6S_8

EuMo_6S_8 has magnetic order at low temperatures (less than 0.4 K), but it seems not to be the simple ferromagnetic order [53]. The seven $4f$ electrons on Eu^{2+} ions are fully spin polarized and completely localized. In this sense, EuMo_6S_8 and BaMo_6S_8 are very similar, except for the breaking of the time-reversal symmetry

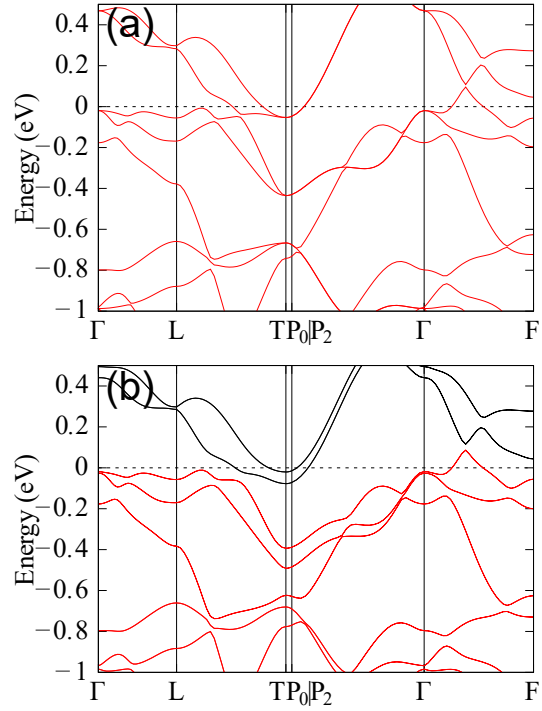


FIG. 8: The band structures of $R\bar{3}$ phase Mo_6S_8 without SOC (a) and with SOC (b). In panel (b), the red bands are the $N - 2$ occupied ones, where N represents the number of valence electrons of BaMo_6S_8 .

and the Kramers degeneracy. Thus, we expect that the \mathbb{Z}_2 topological insulator in BaMo_6S_8 can be driven to axion insulator [54–58], Weyl semimetal [59–63] or trivial magnetic insulator in EuMo_6S_8 . We assumed an artificial ferromagnetic order for both the $R\bar{3}$ and $P\bar{1}$ phases to investigate their topological states.

Now let us consider the $R\bar{3}$ phase firstly. Figure 10 shows the LDA+U band structures of EuMo_6S_8 in the ferromagnetic order. The on-site Hubbard $U = 5$ eV on the f orbitals of Eu is considered. The difference between EuMo_6S_8 and BaMo_6S_8 is the spin splitting in the band structure. The spin splitting is quite small and it does not introduce any band inversion. Therefore, the topological states of EuMo_6S_8 in both the N and $N - 2$ occupation cases are axion

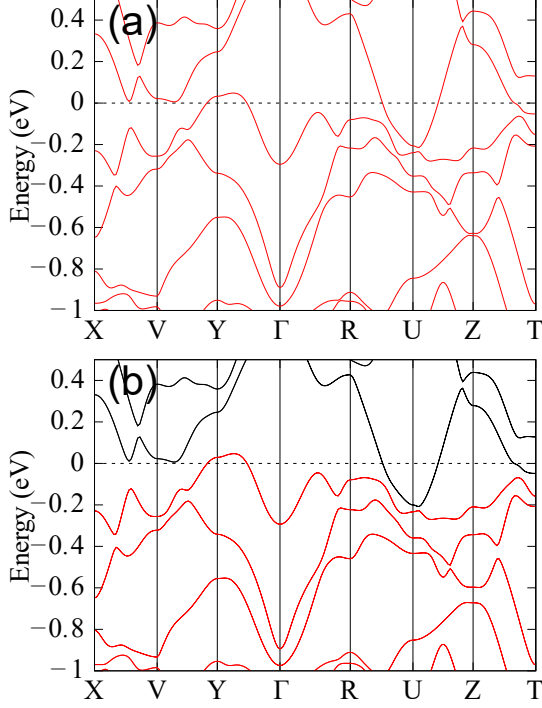


FIG. 9: The band structures of $P\bar{1}$ phase Mo_6S_8 without SOC (a) and with SOC (b). In panel (b), the red bands are the $N - 2$ occupied ones, where N represents the number of valence electrons of BaMo_6S_8 .

insulators as indicated by $z_4 = 2$, which is calculated with SOC according to the formula [64–67]

$$z_4 = \sum_K n_K^- \bmod 4, \quad (1)$$

where n_K^- is the number of occupied bands with odd parity eigenvalues at inversion-invariant momentum K . We also checked our results with increasing U to 6, 7 and 8 eV, and they are not changed.

For the $P\bar{1}$ phase, the band structures are shown in Figs. 11(a) and 11(b). In the $P\bar{1}$ phase, the z_4 indices with SOC are 0 in both of the $N - 2$ and N occupation cases. This difference comes from the additional band inver-

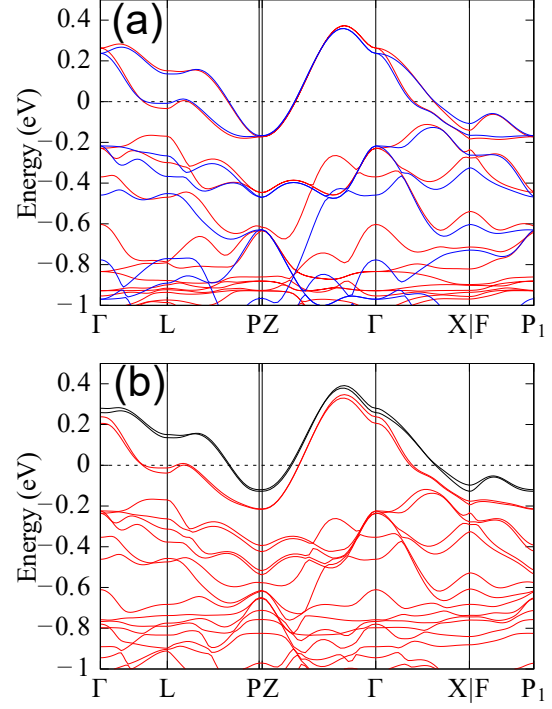


FIG. 10: The band structures of $R\bar{3}$ phase EuMo_6S_8 without SOC (a) and with SOC (b) in ferromagnetic order. In panel (a), the red blue colors represent the spin up and spin down, respectively. In panel (b), the red bands are the N occupied ones, where N represents the number of valence electrons of BaMo_6S_8 . Here, the seven $4f$ electrons of Eu^{2+} are localized and not counted into the valence electrons.

sion caused by structural phase transition from $R\bar{3}$ to $P\bar{1}$ phase. For the N occupation case, at Y (0.0, 0.5, 0.0), the $(N - 1)$ - and N -th bands are inverted with the $(N + 1)$ - and $(N + 2)$ -th bands referring to the $R\bar{3}$ case. The $(N - 1)$ - and N -th bands and the $(N + 1)$ - and $(N + 2)$ -th bands have different parity eigenvalues, leading to the topological trivial state. For the $N - 2$ occupation case, the number of occupied bands with odd parities is reduced by two at V (0.5, 0.5, 0.0), and this results in the topological triv-

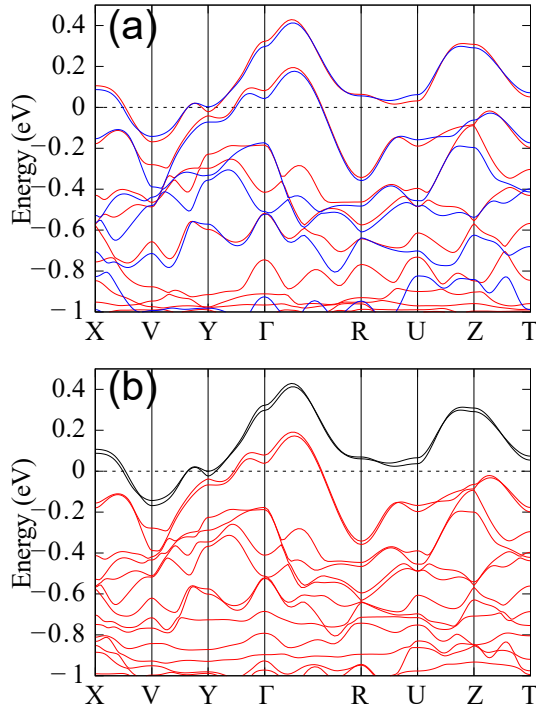


FIG. 11: The band structures of $P\bar{1}$ phase EuMo_6S_8 without SOC (a) and with SOC (b) in ferromagnetic order. In panel (a), the red and blue colors represent the spin up and spin down, respectively. In panel (b), the red bands are the N occupied ones, where N represents the number of valence electrons of BaMo_6S_8 . Here, the seven $4f$ electrons of Eu^{2+} are localized and not counted into the valence electrons.

ial state. Similarly, the topological state of $P\bar{1}$ phase is not changed with increasing U to 6, 7 and 8 eV.

III. CONCLUSION AND DISCUSSION

We systematically studied the topological states of CP materials. For BaMo_6S_8 in both of the $R\bar{3}$ and $P\bar{1}$ phases, the topological \mathbb{Z}_2 indices are $(1; 0, 0, 0)$ in the N occupation and

$(1; 1, 1, 1)$ in the $N - 2$ occupation cases. For $R\bar{3}$ phase SrMo_6S_8 , the topological states are the same as $R\bar{3}$ phase BaMo_6S_8 . For $P\bar{1}$ phase SrMo_6S_8 , it is a strong topological insulator in the N occupation case, with $\mathbb{Z}_2 = (1; 0, 0, 0)$. For the $N - 2$ occupation case, it is close to a topological phase transition point between the strong and weak topological states. For Mo_6S_8 without the divalent metal atoms, it is a topological insulator and the topological invariants are the same as $R\bar{3}$ phase BaMo_6S_8 in the $N - 2$ occupation case. But in the $P\bar{1}$ phase, the topological indices are $(1; 0, 0, 1)$, which are different from the previous compounds because of the further crystal distortion without cation ions A. For EuMo_6S_8 with ferromagnetic order, it is an axion insulator with $z_4 = 2$ in both the N and $N - 2$ occupation cases in the $R\bar{3}$ phase, whereas it is a trivial magnetic insulator in the $P\bar{1}$ phase because of the additional band inversion. The information of topological states of the compounds with time-reversal symmetry can also be seen in the results of the high-throughput searching of topological materials [68–72]. However, some of the results are different from ours because of the difference in detail of calculations, such as the crystal structures and the exchange-correlation functionals. Combining the intriguing physical properties of CP materials, such as high transition temperature and high upper critical field superconductivity, the nontrivial band topology revealed in this work may open another dimension in their research and provide a platform to construct topological superconductivity and Majorana modes.

ACKNOWLEDGMENTS

We acknowledge the supports from the National Natural Science Foundation (Grant No. 11925408, 11921004 and 12188101), the Ministry of Science and Technology of China (Grant No. 2018YFA0305700), the Chinese Academy of Sciences (Grant No. XDB33000000), the Informatization Plan of Chinese Academy of Sciences (Grant No. CAS-WX2021SF-

0102), the K. C. Wong Education Foundation (GJTD-2018-01), the Beijing Natural Science Foundation (Z180008), and the Beijing Municipal Science and Technology Commission

(Z191100007219013). X.D. acknowledges financial support from the Hong Kong Research Grants Council (Project No. GRF16300918 and No. 16309020).

-
- [1] O. Peña, Chevrel phases: Past, present and future, *Phys. C: Supercond. Appl.* **514**, 95 (2015), superconducting Materials: Conventional, Unconventional and Undetermined.
 - [2] R. Chevrel, M. Sergent, and J. Prigent, Sur de nouvelles phases sulfurées ternaires du molybdène, *J. Solid State Chem.* **3**, 515 (1971).
 - [3] M. Marezio, P. Dernier, J. Remeika, E. Corenzwit, and B. Matthias, Superconductivity of ternary sulfides and the structure of PbMo_6S_8 , *Mater. Res. Bull.* **8**, 657 (1973).
 - [4] J. D. Jorgensen and D. G. Hinks, Low temperature structural distortion in the high Tc chevrel-phase superconductors PbMo_6S_8 and SnMo_6S_8 , *Solid State Commun.* **53**, 289 (1985).
 - [5] A. Gupta, M. Decroux, T. Willis, and Ø. Fischer, Resistivity broadening, upper critical fields and irreversibility lines in bulk PbMo_6S_8 and SnMo_6S_8 chevrel phase superconductors, *Physica C: Superconductivity* **235-240**, 2541 (1994).
 - [6] P. Hor, M. Wu, T. Lin, X. Shao, X. Jin, and C. Chu, Pressure induced superconductivity in BaMo_6S_8 , *Solid State Commun.* **44**, 1605 (1982).
 - [7] Y. S. Yao, R. P. Guertin, D. G. Hinks, J. Jorgensen, and D. W. Capone II, Superconductivity of divalent chevrel phases at very high pressures, *Phys. Rev. B* **37**, 5032 (1988).
 - [8] Y. Y. Shu, R. Guertin, D. Capone, and D. Hinks, Upper critical field of the pressure induced superconductor BaMo_6S_8 , *Physica C: Superconductivity* **157**, 247 (1989).
 - [9] M. Decroux, M. S. Torikachvili, M. B. Maple, R. Baillif, Ø. Fischer, and J. Muller, Experimental evidence for bulk superconductive behavior of EuMo_6S_8 under pressure, *Phys. Rev. B* **28**, 6270 (1983).
 - [10] M. Decroux, S. E. Lambert, M. S. Torikachvili, M. B. Maple, R. P. Guertin, L. D. Woolf, and R. Baillif, Observation of bulk superconductivity in EuMo_6S_8 under pressure, *Phys. Rev. Lett.* **52**, 1563 (1984).
 - [11] C. Geantet, J. Padiou, O. Peña, M. Sergent, and R. Horyn, Evidence of superconductivity in $\text{Ca}_x^{2+}\text{Mo}_6\text{S}_8$ single crystals at normal pressure, *Solid State Commun.* **64**, 1363 (1987).
 - [12] K. Ma, K. Gornicka, R. Lefèvre, Y. Yang, H. M. Rønnow, H. O. Jeschke, T. Klimczuk, and F. O. von Rohr, Superconductivity with high upper critical field in the cubic centrosymmetric η -carbide $\text{Nb}_4\text{Rh}_2\text{C}_{1-\delta}$, *ACS Mater. Au* **1**, 55 (2021), <https://doi.org/10.1021/acsmaterialsau.1c00011>.
 - [13] M. Tinkham, *Introduction to Superconductivity*, Dover Books on Physics Series (Dover Publications, 2004).
 - [14] H. W. MEUL, On the unusual physical properties of europium-based molybdenum chalcogenides and related chevrel compounds, *Helv. phys. acta* **59**, 417 (1986).
 - [15] C. Rossel, M. Maple, H. Meul, Ø. Fischer, X. Zhang, and N. Ong, Transport and magnetic properties of BaMo_6S_8 : Some evidence for charge-density waves, *Physica B+C* **135**, 381 (1985).
 - [16] E. P. Stillwell, A. C. Ehrlich, G. N. Kamm, and D. J. Gillespie, Effect of elastic tension on the electrical resistance of HfTe_5 and ZrTe_5 , *Phys. Rev. B* **39**, 1626 (1989).
 - [17] E. Skelton, T. Wieting, S. Wolf, W. Fuller, D. Gubser, T. Francavilla, and F. Levy, Giant resistivity and X-ray diffraction anomalies in low-dimensional ZrTe_5 and HfTe_5 , *Solid State Commun.* **42**, 1 (1982).
 - [18] H. Weng, X. Dai, and Z. Fang, Transition-metal pentatelluride ZrTe_5 and HfTe_5 : A paradigm for large-gap quantum spin hall insulators, *Phys. Rev. X* **4**, 011002 (2014).
 - [19] Y. Zhang, C. Wang, L. Yu, G. Liu, A. Liang, J. Huang, S. Nie, X. Sun, Y. Zhang, B. Shen, J. Liu, H. Weng, L. Zhao, G. Chen, X. Jia, C. Hu, Y. Ding, W. Zhao, Q. Gao, C. Li, S. He, L. Zhao, F. Zhang, S. Zhang, F. Yang, Z. Wang, Q. Peng, X. Dai, Z. Fang, Z. Xu, C. Chen, and X. J. Zhou, Electronic evidence of temperature-induced lifshitz transition and

- topological nature in ZrTe_5 , *Nat. Commun.* **8**, 15512 (2017).
- [20] C. Vaswani, L.-L. Wang, D. H. Mudiyansele, Q. Li, P. M. Lozano, G. D. Gu, D. Cheng, B. Song, L. Luo, R. H. J. Kim, C. Huang, Z. Liu, M. Mootz, I. E. Perakis, Y. Yao, K. M. Ho, and J. Wang, Light-driven raman coherence as a nonthermal route to ultrafast topology switching in a dirac semimetal, *Phys. Rev. X* **10**, 021013 (2020).
- [21] L. Luo, D. Cheng, B. Song, L.-L. Wang, C. Vaswani, P. M. Lozano, G. Gu, C. Huang, R. H. J. Kim, Z. Liu, J.-M. Park, Y. Yao, K. Ho, I. E. Perakis, Q. Li, and J. Wang, A light-induced phononic symmetry switch and giant dissipationless topological photocurrent in ZrTe_5 , *Nat. Mater.* **20**, 329 (2021).
- [22] Z. Wang, P. Zhang, G. Xu, L. K. Zeng, H. Miao, X. Xu, T. Qian, H. Weng, P. Richard, A. V. Fedorov, H. Ding, X. Dai, and Z. Fang, Topological nature of the $\text{FeSe}_{0.5}\text{Te}_{0.5}$ superconductor, *Phys. Rev. B* **92**, 115119 (2015).
- [23] P. Zhang, K. Yaji, T. Hashimoto, Y. Ota, T. Kondo, K. Okazaki, Z. Wang, J. Wen, G. D. Gu, H. Ding, and S. Shin, Observation of topological superconductivity on the surface of an iron-based superconductor, *Science* **360**, 182 (2018).
- [24] Y. Qian, S. Nie, C. Yi, L. Kong, C. Fang, T. Qian, H. Ding, Y. Shi, Z. Wang, H. Weng, and Z. Fang, Topological electronic states in HfRuP family superconductors, *Npj Comput. Mater.* **5**, 121 (2019).
- [25] Y. Xu, Y. Gu, T. Zhang, C. Fang, Z. Fang, X.-L. Sheng, and H. Weng, Topological nodal lines and hybrid weyl nodes in YCoC_2 , *APL Mater.* **7**, 101109 (2019), <https://doi.org/10.1063/1.5123222>.
- [26] G. Kresse and J. Furthmüller, Efficient iterative schemes for ab initio total-energy calculations using a plane-wave basis set, *Phys. Rev. B* **54**, 11169 (1996).
- [27] G. Kresse and J. Furthmüller, Efficiency of ab-initio total energy calculations for metals and semiconductors using a plane-wave basis set, *Comput. Mater. Sci.* **6**, 15 (1996).
- [28] P. E. Blöchl, Projector augmented-wave method, *Phys. Rev. B* **50**, 17953 (1994).
- [29] G. Kresse and D. Joubert, From ultrasoft pseudopotentials to the projector augmented-wave method, *Phys. Rev. B* **59**, 1758 (1999).
- [30] J. P. Perdew, K. Burke, and M. Ernzerhof, Generalized gradient approximation made simple, *Phys. Rev. Lett.* **77**, 3865 (1996).
- [31] J. Heyd, G. E. Scuseria, and M. Ernzerhof, Hybrid functionals based on a screened coulomb potential, *J. Chem. Phys.* **118**, 8207 (2003), <https://doi.org/10.1063/1.1564060>.
- [32] J. Heyd and G. E. Scuseria, Efficient hybrid density functional calculations in solids: Assessment of the heyd-scuseria-ernzerhof screened coulomb hybrid functional, *J. Chem. Phys.* **121**, 1187 (2004), <https://doi.org/10.1063/1.1760074>.
- [33] J. Vidal, X. Zhang, L. Yu, J.-W. Luo, and A. Zunger, False-positive and false-negative assignments of topological insulators in density functional theory and hybrids, *Phys. Rev. B* **84**, 041109 (2011).
- [34] G. Pizzi, V. Vitale, R. Arita, S. Blügel, F. Freimuth, G. Géranton, M. Gibertini, D. Gresch, C. Johnson, T. Koretsune, J. Ibañez-Azpiroz, H. Lee, J.-M. Lihm, D. Marchand, A. Marrazzo, Y. Mokrousov, J. I. Mustafa, Y. Nohara, Y. Nomura, L. Paulatto, S. Poncé, T. Ponweiser, J. Qiao, F. Thöle, S. S. Tsirkin, M. Wierzbowska, N. Marzari, D. Vanderbilt, I. Souza, A. A. Mostofi, and J. R. Yates, Wannier90 as a community code: new features and applications, *J. Phys. Condens. Matter* **32**, 165902 (2020).
- [35] R. Yu, X. L. Qi, A. Bernevig, Z. Fang, and X. Dai, Equivalent expression of \mathbb{Z}_2 topological invariant for band insulators using the non-abelian berry connection, *Phys. Rev. B* **84**, 075119 (2011).
- [36] Q. Wu, S. Zhang, H.-F. Song, M. Troyer, and A. A. Soluyanov, Wanniertools : An open-source software package for novel topological materials, *Comput. Phys. Commun.* **224**, 405 (2018).
- [37] J. D. Jorgensen and D. G. Hinks, Rhombohedral-to-triclinic phase transition in BaMo_6S_8 , *Physica B+C* **136**, 485 (1986), neutron Scattering.
- [38] S. Zhang, T. Zhang, H. Deng, Y. Ding, Y. Chen, and H. Weng, Crystal and electronic structure of GaTa_4Se_8 from first-principles calculations, *Phys. Rev. B* **102**, 214114 (2020).
- [39] W. Kalsbach, *Strukturelle Phasenübergänge und druckinduzierte Supraleitung von Molybdän-Clusterverbindungen (Chevrel-Phasen)*, Tech. Rep. Juel-1921 (Jülich, 1984).
- [40] B. Koppellhuber-Bitschnau, F. A. Mautner, and K. Yvon, Low-temperature structural phase transition in SrMo_6S_8 studied by x-ray

- powder diffraction, *Monatshefte für Chemie / Chemical Monthly* **121**, 505 (1990).
- [41] Mo6S8 (Mo3S4 rhom) crystal structure: Datasheet from “pauling file multinaries edition – 2012” in *springermaterials*, copyright 2016 Springer-Verlag Berlin Heidelberg & Material Phases Data System (MPDS), Switzerland & National Institute for Materials Science (NIMS), Japan.
- [42] W. R. McKinnon and J. R. Dahn, Structure and electrochemistry of $\text{Li}_x\text{Mo}_6\text{S}_8$, *Phys. Rev. B* **31**, 3084 (1985).
- [43] H. Fukuoka, K. Masuoka, T. Hanaoka, and K. Inumaru, New polymorph of mo_3s_4 prepared using a high-pressure synthesis technique: Crystal structure, electronic property, and band calculation, *Inorg. Chem.* **52**, 7918 (2013).
- [44] Ø. Fischer, A. Treyvaud, R. Chevrel, and M. Sergent, Superconductivity in the $\text{Re}_x\text{Mo}_6\text{S}_8$, *Solid State Commun.* **17**, 721 (1975).
- [45] S. Quezel, P. Burlet, A. Dinia, J. Rossat-Mignod, R. Horyn, O. Pena, and M. Sergent, Neutron diffraction study of the crystal and magnetic structures of $^{153}\text{EuMo}_6\text{S}_8$, *Phys. B: Condens. Matter* **156-157**, 780 (1989).
- [46] See supplemental material at [] for the crystal structure, description of the procedure of band structure renormalization, and more information about the band topology.
- [47] H. Nohl, W. Klose, and O. K. Andersen, Band structures of $\text{M}_x\text{Mo}_6\text{X}_8$ - and $\text{M}_2\text{Mo}_6\text{X}_6$ -cluster compounds, in *Superconductivity in Ternary Compounds I: Structural, Electronic, and Lattice Properties*, edited by Ø. Fischer and M. B. Maple (Springer Berlin Heidelberg, Berlin, Heidelberg, 1982) pp. 165–221.
- [48] El-Batanouny, M. and Wooten, F., *Symmetry and Condensed Matter Physics: A Computational Approach* (Cambridge University Press, 2008).
- [49] H. Watanabe, H. C. Po, M. P. Zaletel, and A. Vishwanath, Filling-enforced gaplessness in band structures of the 230 space groups, *Phys. Rev. Lett.* **117**, 096404 (2016).
- [50] R. Chen, H. C. Po, J. B. Neaton, and A. Vishwanath, Topological materials discovery using electron filling constraints, *Nat. Phys.* **14**, 55 (2018).
- [51] L. Fu and C. L. Kane, Topological insulators with inversion symmetry, *Phys. Rev. B* **76**, 045302 (2007).
- [52] Z. Song, T. Zhang, and C. Fang, Diagnosis for nonmagnetic topological semimetals in the absence of spin-orbital coupling, *Phys. Rev. X* **8**, 031069 (2018).
- [53] T. Takabatake, R. W. McCallum, M. Kubota, and F. Pobell, Low-temperature magnetic properties of EuMo_6S_8 and EuMo_6Se_8 , *J. Low Temp. Phys.* **55**, 111 (1984).
- [54] R. D. Peccei and H. R. Quinn, CP conservation in the presence of pseudoparticles, *Phys. Rev. Lett.* **38**, 1440 (1977).
- [55] A. M. Essin, J. E. Moore, and D. Vanderbilt, Magnetoelectric polarizability and axion electrodynamics in crystalline insulators, *Phys. Rev. Lett.* **102**, 146805 (2009).
- [56] J. Langbehn, Y. Peng, L. Trifunovic, F. von Oppen, and P. W. Brouwer, Reflection-symmetric second-order topological insulators and superconductors, *Phys. Rev. Lett.* **119**, 246401 (2017).
- [57] A. M. Essin, J. E. Moore, and D. Vanderbilt, Magnetoelectric polarizability and axion electrodynamics in crystalline insulators, *Phys. Rev. Lett.* **102**, 146805 (2009).
- [58] Y. Xu, Z. Song, Z. Wang, H. Weng, and X. Dai, Higher-order topology of the axion insulator EuIn_2As_2 , *Phys. Rev. Lett.* **122**, 256402 (2019).
- [59] H. Weng, C. Fang, Z. Fang, B. A. Bernevig, and X. Dai, Weyl semimetal phase in non-centrosymmetric transition-metal monophosphides, *Phys. Rev. X* **5**, 011029 (2015).
- [60] B. Q. Lv, H. M. Weng, B. B. Fu, X. P. Wang, H. Miao, J. Ma, P. Richard, X. C. Huang, L. X. Zhao, G. F. Chen, Z. Fang, X. Dai, T. Qian, and H. Ding, Experimental discovery of weyl semimetal TaAs, *Phys. Rev. X* **5**, 031013 (2015).
- [61] X. Wan, A. M. Turner, A. Vishwanath, and S. Y. Savrasov, Topological semimetal and fermi-arc surface states in the electronic structure of pyrochlore iridates, *Phys. Rev. B* **83**, 205101 (2011).
- [62] G. Xu, H. Weng, Z. Wang, X. Dai, and Z. Fang, Chern semimetal and the quantized anomalous hall effect in HgCr_2Se_4 , *Phys. Rev. Lett.* **107**, 186806 (2011).
- [63] Y. Hu, C. Yue, D. Yuan, J. Gao, Z. Huang, Z. Fang, C. Fang, H. Weng, and W. Zhang, The evolution of Weyl nodes in Ni doped thallium niobate pyrochlore $\text{Tl}_{2-x}\text{Ni}_x\text{Nb}_2\text{O}_7$, arXiv e-prints, arXiv:2112.04127 (2021), arXiv:2112.04127 [cond-mat.mtrl-sci].

- [64] A. M. Turner, Y. Zhang, R. S. K. Mong, and A. Vishwanath, Quantized response and topology of magnetic insulators with inversion symmetry, *Phys. Rev. B* **85**, 165120 (2012).
- [65] H. Watanabe, H. C. Po, and A. Vishwanath, Structure and topology of band structures in the 1651 magnetic space groups, *Sci. Adv.* **4**, eaat8685 (2018).
- [66] S. Ono and H. Watanabe, Unified understanding of symmetry indicators for all internal symmetry classes, *Phys. Rev. B* **98**, 115150 (2018).
- [67] Y. Xu, L. Elcoro, Z.-D. Song, B. J. Wieder, M. G. Vergniory, N. Regnault, Y. Chen, C. Felser, and B. A. Bernevig, High-throughput calculations of magnetic topological materials, *Nature* **586**, 702 (2020).
- [68] B. Bradlyn, L. Elcoro, J. Cano, M. G. Vergniory, Z. Wang, C. Felser, M. I. Aroyo, and B. A. Bernevig, Topological quantum chemistry, *Nature* **547**, 298 (2017).
- [69] M. G. Vergniory, L. Elcoro, C. Felser, N. Regnault, B. A. Bernevig, and Z. Wang, A complete catalogue of high-quality topological materials, *Nature* **566**, 480 (2019).
- [70] M. G. Vergniory, B. J. Wieder, L. Elcoro, S. S. P. Parkin, C. Felser, B. A. Bernevig, and N. Regnault, All topological bands of all nonmagnetic stoichiometric materials, *Science* **376**, eabg9094 (2022).
- [71] T. Zhang, Y. Jiang, Z. Song, H. Huang, Y. He, Z. Fang, H. Weng, and C. Fang, Catalogue of topological electronic materials, *Nature* **566**, 475 (2019).
- [72] F. Tang, H. C. Po, A. Vishwanath, and X. Wan, Comprehensive search for topological materials using symmetry indicators, *Nature* **566**, 486 (2019).

Supplementary Materials: Topological States in Chevrel Phase Materials from First-principle Calculations

Shuai Zhang,^{1,2} Shiyu Peng,^{1,2} Xi Dai,³ and Hongming Weng^{1,2,4,*}

¹*Beijing National Laboratory for Condensed Matter Physics,
and Institute of Physics, Chinese Academy of Sciences, Beijing 100190, China*

²*University of Chinese Academy of Sciences, Beijing 100049, China*

³*Department of Physics, Hong Kong University of Science and Technology, Clear Water Bay, Hong Kong*

⁴*Songshan Lake Materials Laboratory, Dongguan, Guangdong 523808, China*

* hmweng@iphy.ac.cn

I. THE PROCEDURE OF BAND RENORMALIZATION

Suppose our aim is to get a global gap between the N lowest bands and the $(N+1)$ -th band (i.e., a global gap in the N occupation case) at the reference energy ε_0 . We define $m_k = (E_{N+1,k} + E_{N,k})/2$ as the middle point of the N - and the $(N+1)$ -th bands at k , where $E_{N,k}$ is the energy of the N -th band. Then, we define $\delta_k = \varepsilon_0 - m_k$. After shifting the energy of all the bands at k with δ_k , we can get a global gap at the reference energy ε_0 . For convenience, we call this procedure “renormalization”. There is no band inversion at each k point during this procedure. Thus, this kind of renormalization does not affect the band topology.

II. THE PARITY DISTRIBUTION, WCCS AND SURFACE STATES OF BaMo₆S₈

In Fig. S1, we show the parity distribution and WCCs of $R\bar{3}$ phase BaMo₆S₈ with SOC in the $N-2$ occupation, N occupation and $N+2$ occupation cases, respectively. These results indicate that the \mathbb{Z}_2 indices of $R\bar{3}$ phase BaMo₆S₈ are $(1; 0, 0, 0)$ in the N occupation case and $(1; 1, 1, 1)$ in the $N-2$ occupation case. Fig. S1c, S1f, S1i and S1l demonstrate that the the lowest $N+2$ bands are topologically trivial, as we mentioned in the main text.

In Fig. S2, we show the parity distribution and WCCs of $P\bar{1}$ phase BaMo₆S₈ with SOC in the $N-2$ occupation, N occupation and $N+2$ occupation cases, respectively. These results indicate that the \mathbb{Z}_2 indices of $P\bar{1}$ phase BaMo₆S₈ are the same as the ones of $R\bar{3}$ phase BaMo₆S₈ in both of the $N-2$ and N occupation cases. Fig. S2c, S2f, S2i and S2l demonstrate that the the lowest $N+2$ bands are topologically trivial.

The (001) surface states of $P\bar{1}$ phase BaMo₆S₈ with SOC are shown in Fig. S3a. Because of the absence of global gap in both of the N and $N-2$ occupation cases, the surface Dirac cone is mixed with the bulk states. We calculated the renormalized band structures and the corresponding surface states with 0.02 eV and 0.01 eV onsite energy correction to the atoms in the surface region for the N occupation and $N-2$ occupation cases, respectively. As shown in Fig. S3b and S3c, there is a global gap in bulk states and clear surface Dirac cones in both cases. There is only one surface Dirac cone at $\bar{\Gamma}$ in the N occupation case and three surface Dirac cones at \bar{X} , $\bar{\Gamma}$ and \bar{X}_1 in the $N-2$ occupation case. The number and the distribution of surface Dirac cones are consistent with the parity distribution.

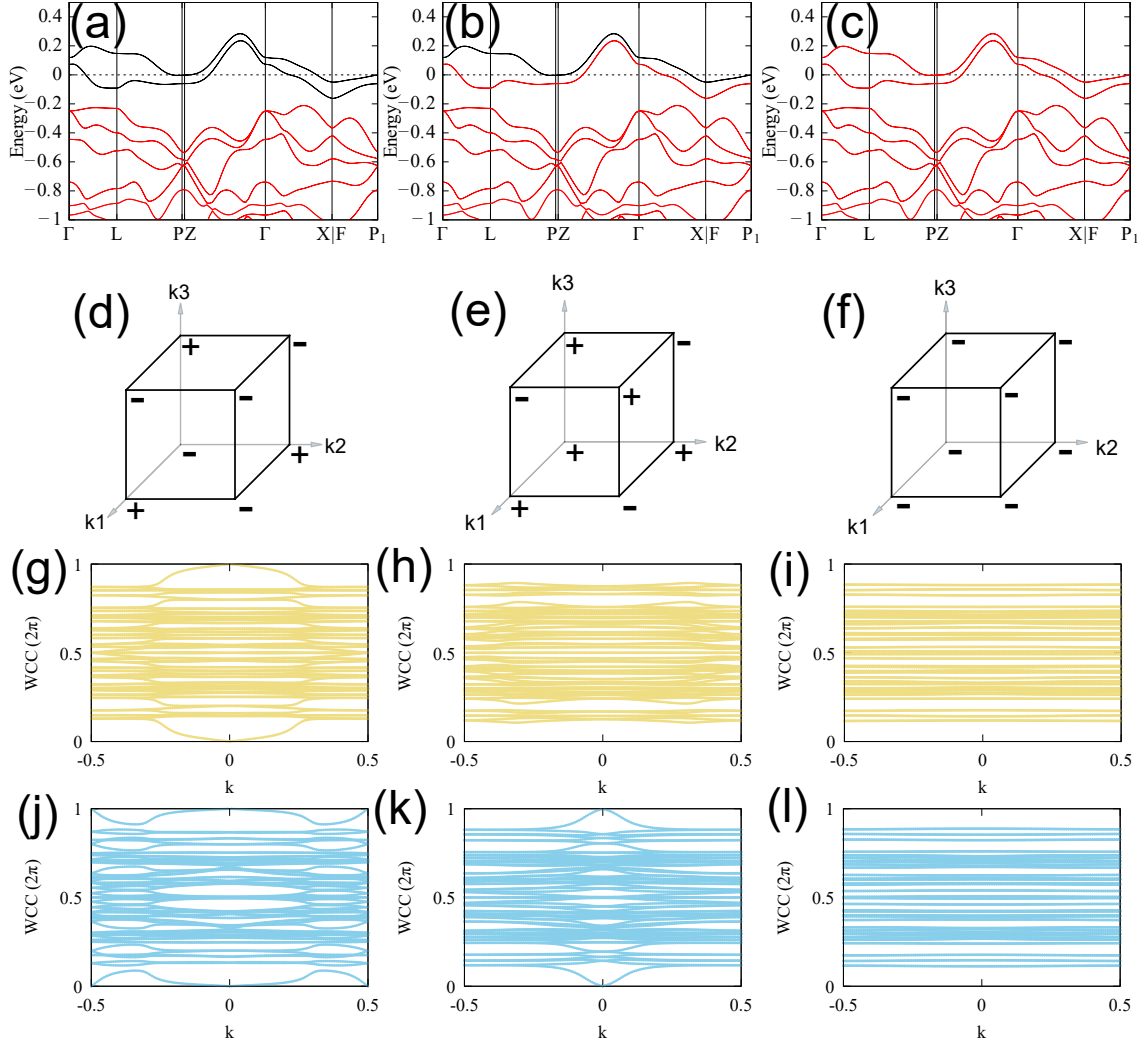


FIG. S1: The band structures, parities, WCCs of $R\bar{3}$ phase BaMo_6S_8 in different occupation cases with SOC. Here, each column belongs to the same occupation case. In (a), (b) and (c), the red bands represent the occupied ones, which show the $N - 2$ occupation, N occupation, and $N + 2$ occupation cases intuitively. In (d), (e) and (f), “-” represents the product of parity eigenvalues of all occupied Kramers degenerate pairs at this TRIM to be odd, and “+” represents even. (g), (h), (i) show the evolution of WCCs on the $k_3 = \pi$ plane, and Fig. (j), (k), (l) show the evolution of WCCs on the $k_3 = 0$ plane. Here, the WCCs integral direction is k_1 and WCCs evolve along k_2 .

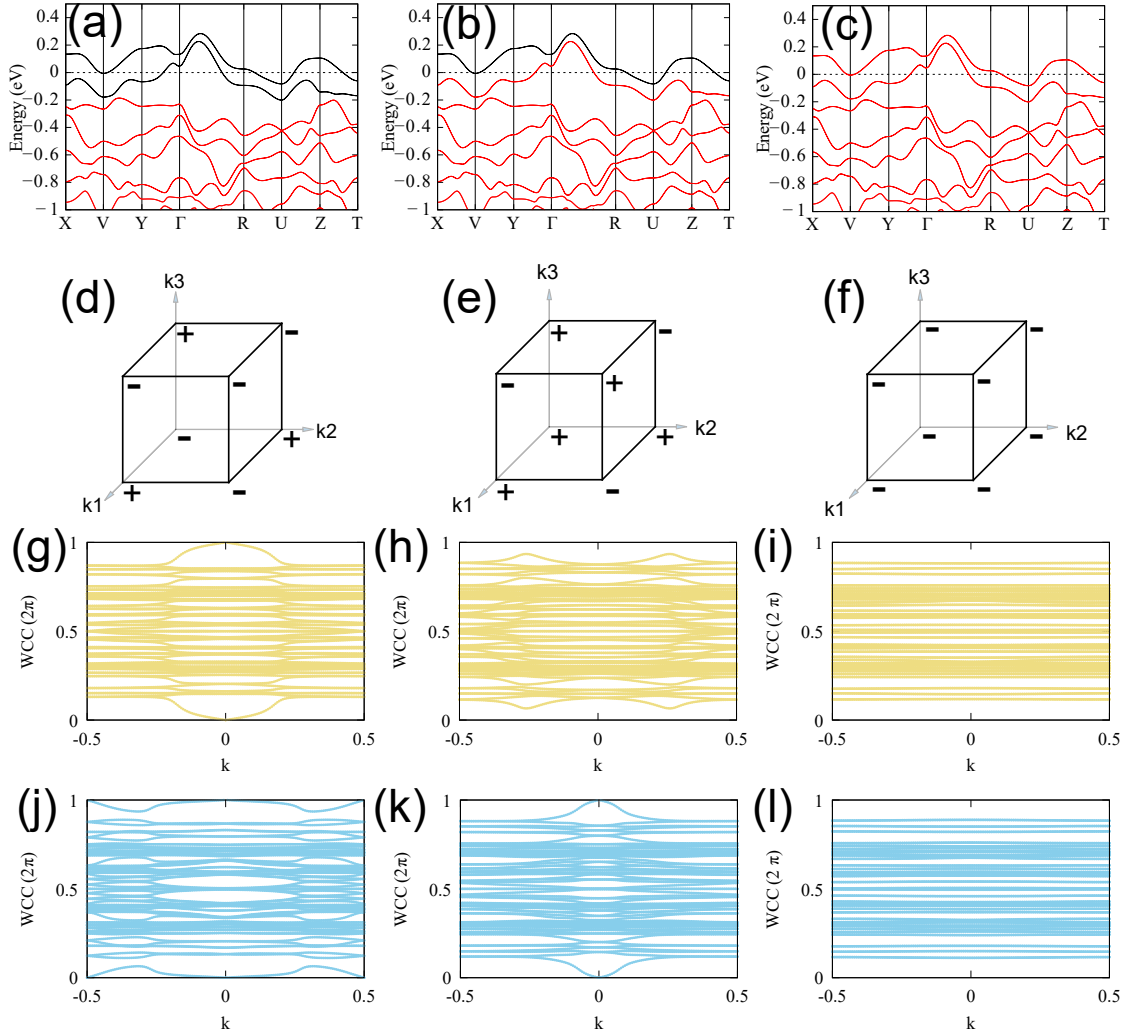


FIG. S2: The band structures, parities, WCCs of $P\bar{1}$ phase BaMo_6S_8 in different occupation cases with SOC. Here, each column belongs to the same occupation case. In (a), (b) and (c), the red bands represent the occupied ones, which show the $N - 2$ occupation, N occupation, and $N + 2$ occupation cases intuitively. In (d), (e) and (f), “-” represents the product of parity eigenvalues of all occupied Kramers degenerate pairs at this TRIM to be odd, and “+” represents even. (g), (h), (i) show the evolution of WCCs on the $k_3 = \pi$ plane, and (j), (k), (l) show the evolution of WCCs on the $k_3 = 0$ plane. Here, the WCCs integral direction is k_1 and WCCs evolves along k_2 .

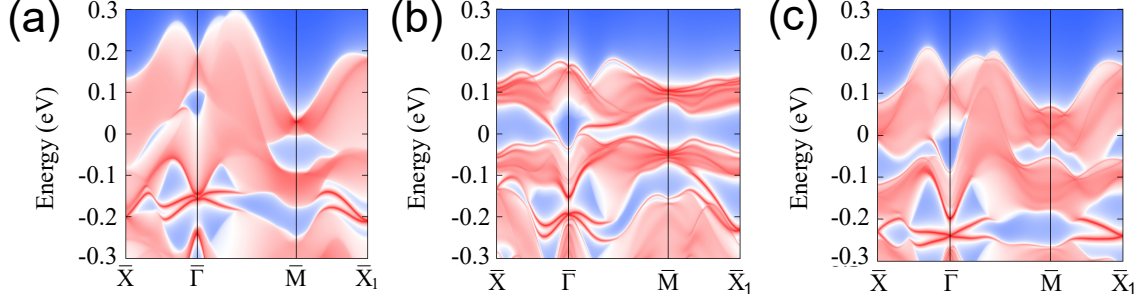


FIG. S3: The (001) surface states of $P\bar{1}$ phase BaMo_6S_8 with SOC. (a) The surface states calculated with the original band structure. (b) The surface states calculated with the renormalized band structure, which has a global gap in the N occupation case. (c) The surface states calculated with the renormalized band structure, which has a global gap in the $N - 2$ occupation case.

III. THE BAND STRUCTURE, PARITY DISTRIBUTION, WCCS AND SURFACE STATES OF SrMo_6S_8

Fig. S4 shows the band structures of $R\bar{3}$ phase SrMo_6S_8 , which are basically the same as the ones of $R\bar{3}$ phase BaMo_6S_8 .

In Fig. S5, we show the parity distribution and WCCs of $R\bar{3}$ phase SrMo_6S_8 with SOC in the $N - 2$ occupation, N occupation and $N + 2$ occupation cases, respectively. These results indicate that the \mathbb{Z}_2 indices of $R\bar{3}$ phase SrMo_6S_8 are $(1; 0, 0, 0)$ in the N occupation case and $(1; 1, 1, 1)$ in the $N - 2$ occupation case. Fig. S5c, S5f, S5i and S5l demonstrate that the lowest $N + 2$ bands are topologically trivial.

The (001) surface states of $R\bar{3}$ phase SrMo_6S_8 with SOC are shown in Fig. S6a. Because of the absence of global gap in both of the N and $N - 2$ occupation cases, the surface Dirac cone is mixed with the bulk states. We calculated the renormalized band structures and the corresponding surface states with 0.02 eV onsite energy correction to the atoms in the surface region for the N occupation and $N - 2$ occupation cases, respectively. As shown in Fig. S6b and S6c, there is a global gap in bulk states and clear surface Dirac cones in both cases. There is only one surface Dirac cone at $\bar{\Gamma}$ in the N occupation case and three surface Dirac cones at \bar{X} , $\bar{\Gamma}$ and \bar{X}_1 in the $N - 2$ occupation case. The number and the distribution of surface Dirac cones are consistent with the parity distribution.

The parity distribution and WCCs of $P\bar{1}$ phase SrMo_6S_8 with SOC in the N occupation case are shown in Fig. S7. These results show that the \mathbb{Z}_2 indices of $P\bar{1}$ phase SrMo_6S_8 are $(1; 0, 0, 0)$ in the N occupation case.

The three Mo-S bond lengths in $P\bar{1}$ phase BaMo_6S_8 and SrMo_6S_8 are shown in Fig. S8 to compare the difference in their crystal structures.

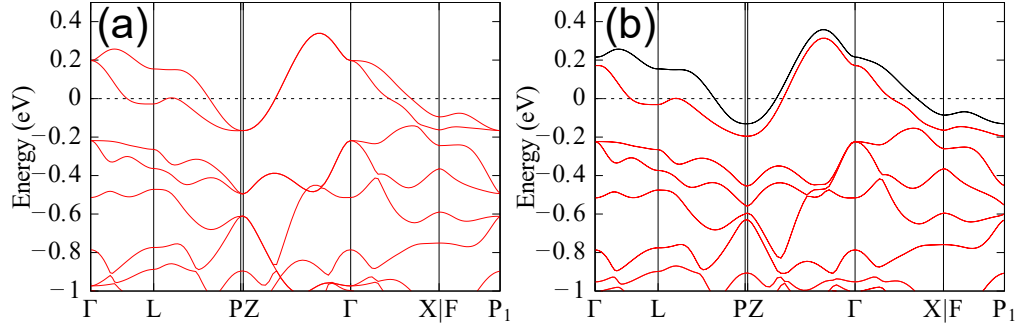


FIG. S4: The band structures of $R\bar{3}$ phase SrMo_6S_8 without SOC (a) and with SOC (b). In (b), the red bands are the N occupied ones, where N represents the number of valence electrons of BaMo_6S_8 .

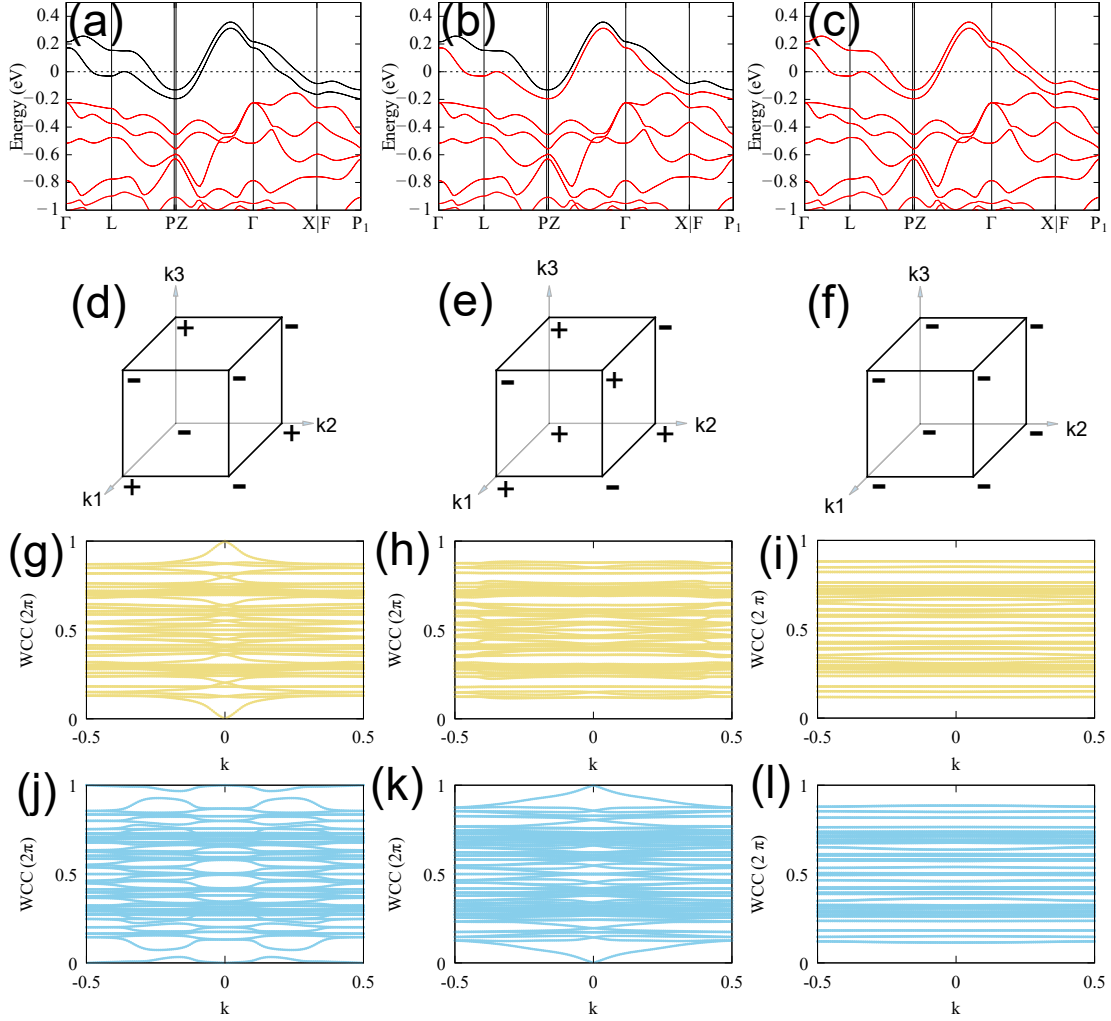


FIG. S5: The band structures, parities, WCC of $R\bar{3}$ SrMo_6S_8 in different occupation cases with SOC. Here, each column belongs to the same occupation case. In (a), (b) and (c), the red bands represent the occupied ones, which show the $N - 2$ occupation, N occupation, and $N + 2$ occupation cases intuitively. In (d), (e) and (f), “-” represents the product of parity eigenvalues of all occupied Kramers degenerate pairs at this TRIM to be odd, and “+” represents even. (g), (h), (i) show the evolution of WCCs on the $k_3 = \pi$ plane, and (j), (k), (l) show the evolution of WCC on the $k_3 = 0$ plane. Here, the WCCs integral direction is k_1 and WCCs evolve along k_2 .

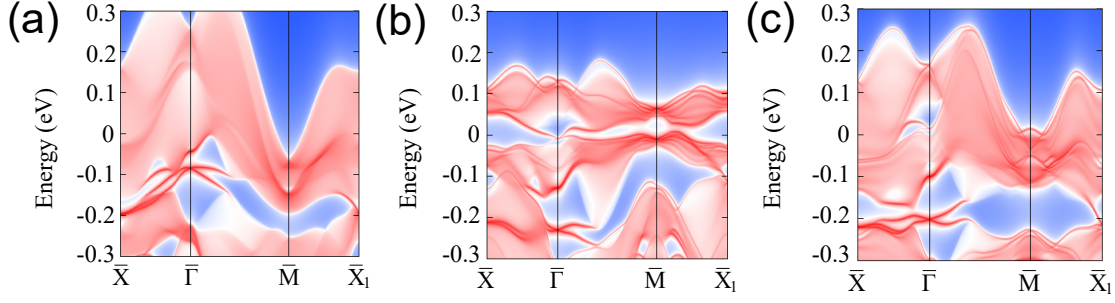


FIG. S6: The (001) surface states of $R\bar{3}$ phase SrMo_6S_8 with SOC. (a) The surface states calculated with the original band structure. (b) The surface states calculated with the renormalized band structure, which has a global gap in the N occupation case. (c) The surface states calculated with the renormalized band structure, which has a global gap in the $N - 2$ occupation case.

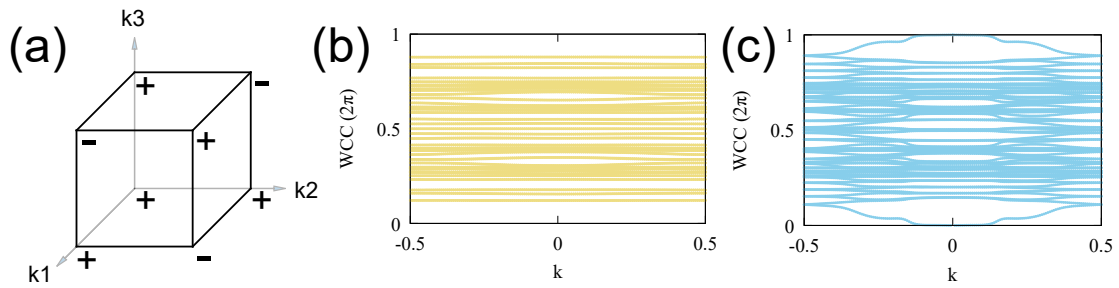


FIG. S7: The information of the topological state of $P\bar{1}$ phase SrMo_6S_8 with SOC. (a) The parity distribution, where the “+” represents even and the “-” represents odd. (b) and (c) show the evolution of WCCs on the $k_3 = \pi$ plane and the $k_3 = 0$ plane, respectively. Here, the WCCs integral direction is k_1 and WCCs evolve along k_2 .

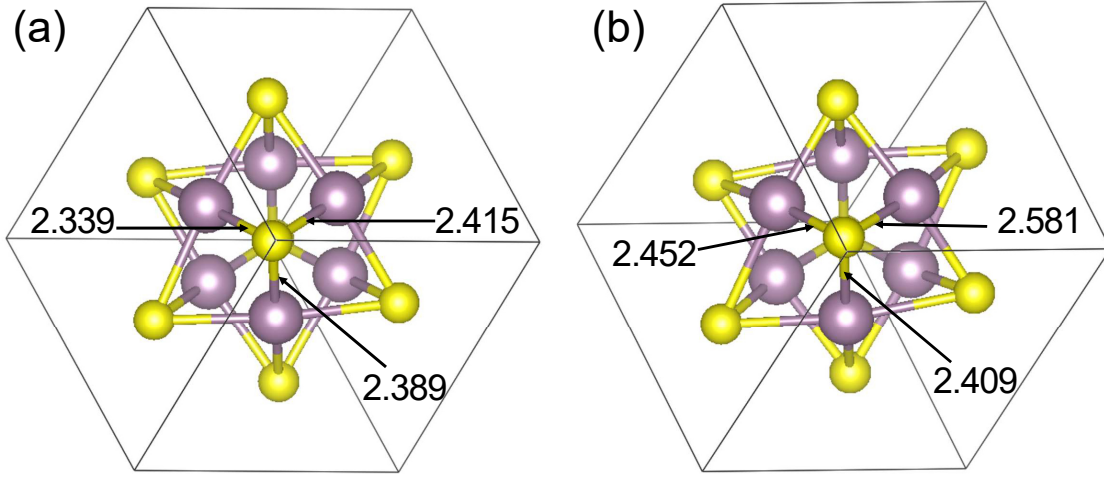


FIG. S8: The Mo_6S_8 clusters of BaMo_6S_8 (a) and SrMo_6S_8 (b) in the $P\bar{1}$ phase and the three bond lengths (in unit Å) is labeled. Here we omitted the Ba (Sr) atoms for clearness.

IV. THE PARITY DISTRIBUTION, WCCS AND SURFACE STATES OF Mo_6S_8

In Fig. S9, we show the parity distribution and WCCs of $R\bar{3}$ phase Mo_6S_8 with SOC. These results show that the \mathbb{Z}_2 indices of $R\bar{3}$ phase Mo_6S_8 are $(1; 0, 0, 0)$, which are the same as the ones of $R\bar{3}$ phase BaMo_6S_8 in the $N - 2$ occupation case.

The (001) surface states of $R\bar{3}$ phase Mo_6S_8 are shown in Fig. S10a. Because of the absence of global gap, the surface Dirac cone is mixed with the bulk states. We calculated the renormalized band structure, which has a global gap, and the corresponding surface states, as shown in Fig. S10b. There are three surface Dirac cones at \bar{X} , $\bar{\Gamma}$ and \bar{X}_1 . The number and the distribution of surface Dirac cones are consistent with the parity distribution.

The parity distribution with SOC of $P\bar{1}$ phase Mo_6S_8 is shown in Fig. S11, which indicates the \mathbb{Z}_2 indices of $P\bar{1}$ phase Mo_6S_8 are $(1; 0, 0, 1)$.

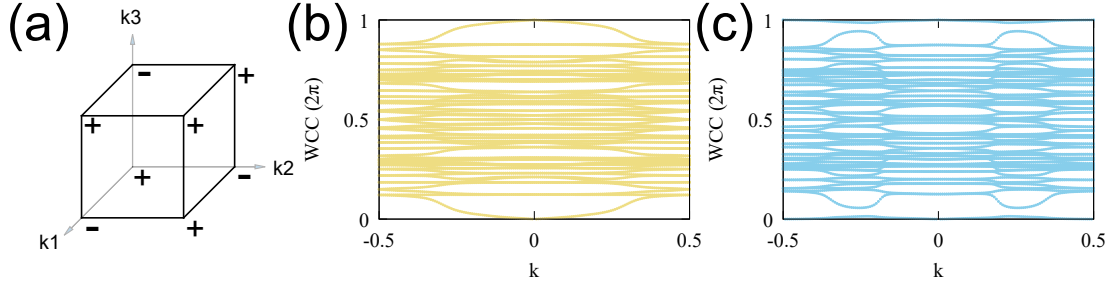


FIG. S9: The information of the topological states of $R\bar{3}$ phase Mo_6S_8 with SOC. (a) The parity distribution, where “+” represents even and “-” represents odd. (b) and (c) show the evolution of WCCs on the $k_3 = \pi$ plane and the $k_3 = 0$ plane, respectively. Here, the WCCs integral direction is k_1 and WCCs evolve along k_2 .

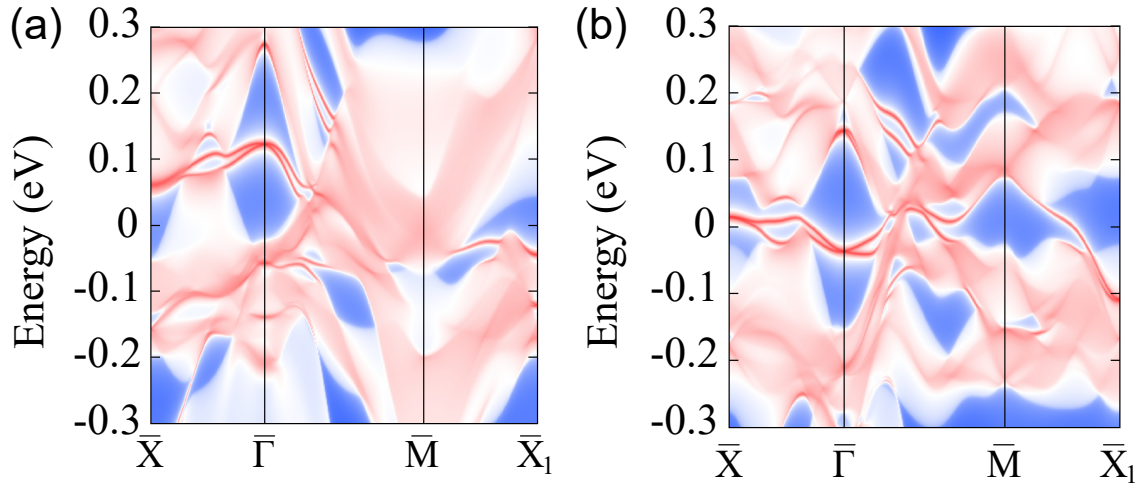


FIG. S10: The (001) surface states of $R\bar{3}$ phase Mo_6S_8 with SOC. (a) The surface states calculated with the original band structure. (b) The surface states calculated with the renormalized band structure with a global gap.

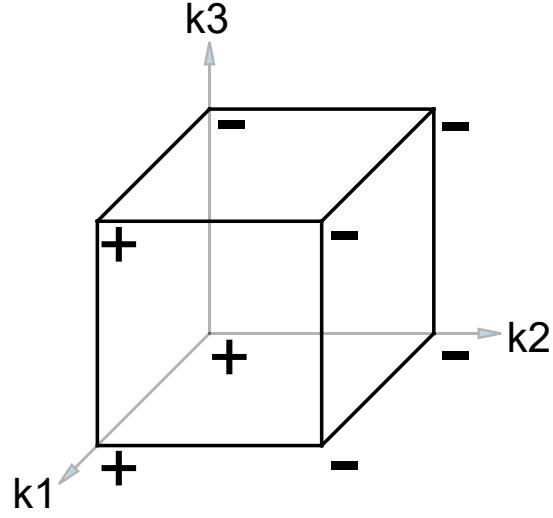


FIG. S11: The parity distribution of $P\bar{1}$ phase Mo_6S_8 with SOC, where “+” represents even, and “-” represents odd.

V. THE CRYSTAL STRUCTURES OF BaMo_6S_8 , SrMo_6S_8 , Mo_6S_8 AND EuMo_6S_8

We list the crystal structures used in calculations in Tab. I- IV.

TABLE I: The crystal structures of BaMo_6S_8 in the $R\bar{3}$ phase (ICDD PDF: 01-088-1169) [1] and the $P\bar{1}$ phase (ICDD PDF: 01-088-1170) [1].

	BaMo_6S_8					
	$R\bar{3}$			$P\bar{1}$		
Lattice vectors (\AA)						
a	4.64870	2.68393	3.92447	-6.56850	0.00000	0.00000
b	-4.64870	2.68393	3.92447	-0.11946	-0.12586	-6.69535
c	0.00000	-5.36786	3.92447	-0.24048	-6.65015	0.00000
Atom positions (fraction)						
Ba	0.00000	0.00000	0.00000	0.00000	0.00000	0.00000
Mo	0.76541	0.43444	0.58245	-0.58084	-0.76250	-0.43557
Mo	0.23459	0.56556	0.41755	-0.41916	-0.23750	-0.56443
Mo	0.56556	0.41755	0.23459	-0.43472	-0.58235	-0.76695
Mo	0.58245	0.76541	0.43444	-0.56528	-0.41765	-0.23305
Mo	0.41755	0.23459	0.56556	-0.76736	-0.43322	-0.58331
Mo	0.43444	0.58245	0.76541	-0.23264	-0.56678	-0.41669
S	0.60969	0.26402	0.87703	-0.26310	-0.87600	-0.60760
S	0.39031	0.73598	0.12297	-0.73690	-0.12400	-0.39240
S	0.73598	0.12297	0.39031	-0.74760	-0.74440	-0.75310
S	0.87703	0.60969	0.26402	-0.25240	-0.25560	-0.24690
S	0.12297	0.39031	0.73598	-0.87530	-0.60850	-0.26410
S	0.26402	0.87703	0.60969	-0.12470	-0.39150	-0.73590
S	0.74850	0.74850	0.74850	-0.61220	-0.26240	-0.87760
S	0.25150	0.25150	0.25150	-0.38780	-0.73760	-0.12240

TABLE II: The crystal structures of SrMo_6S_8 in the $R\bar{3}$ phase (ICDD PDF: 01-085-9202) [2] and the $P\bar{1}$ phase (ICDD PDF: 04-001-6572) [3].

	SrMo ₆ S ₈					
	$R\bar{3}$			$P\bar{1}$		
Lattice vectors (Å)						
a	4.59480	2.65281	3.84773	-6.48100	0.00000	0.00000
b	-4.59480	2.65281	3.84773	-0.08030	-0.08447	-6.60997
c	0.00000	-5.30562	3.84773	-0.20999	-6.56864	0.00000
Atom positions (fraction)						
Sr	0.00000	0.00000	0.00000	0.00000	0.00000	0.00000
Mo	0.22900	0.41799	0.56300	-0.23100	-0.41700	-0.56400
Mo	0.77100	0.58201	0.43700	-0.76900	-0.58300	-0.43600
Mo	0.56300	0.22900	0.41799	-0.41800	-0.56800	-0.23200
Mo	0.43700	0.77100	0.58201	-0.58200	-0.43200	-0.76800
Mo	0.41799	0.56300	0.22900	-0.56700	-0.22600	-0.41800
Mo	0.58201	0.43700	0.77100	-0.43300	-0.77400	-0.58200
S	0.38400	0.12801	0.74100	-0.12600	-0.76500	-0.38500
S	0.61600	0.87199	0.25900	-0.87400	-0.23500	-0.61500
S	0.74100	0.38400	0.12801	-0.23200	-0.22500	-0.25500
S	0.25900	0.61600	0.87199	-0.76800	-0.77500	-0.74500
S	0.12801	0.74100	0.38400	-0.37300	-0.12300	-0.71800
S	0.87199	0.25900	0.61600	-0.62700	-0.87700	-0.28200
S	0.24700	0.24700	0.24700	-0.74800	-0.35900	-0.14400
S	0.75300	0.75300	0.75300	-0.25200	-0.64100	-0.85600

TABLE III: Information of the crystal structures of Mo_6S_8 in the $R\bar{3}$ phase (SpringerMaterials Dataset ID: sd_0312550) [4, 5] and the $P\bar{1}$ phase (ICDD PDF: 04-020-4062) [6].

	Mo ₆ S ₈					
	$R\bar{3}$			$P\bar{1}$		
Lattice vectors (Å)						
a	4.59460	2.65269	3.62933	1.59392	-6.41288	0.00000
b	-4.59460	2.65269	3.62933	6.36400	0.00000	0.00000
c	0.00000	-5.30539	3.62933	3.19332	-2.47343	5.49467
Atom positions (fraction)						
Mo	0.77696	0.58703	0.45392	-0.00147	-0.22401	0.50321
Mo	0.22304	0.41297	0.54608	-0.99853	0.22401	0.49679
Mo	0.45392	0.77696	0.58703	-0.48276	0.27235	0.18129
Mo	0.54608	0.22304	0.41297	-0.51724	-0.27235	0.81871
Mo	0.58703	0.45392	0.77696	-0.48563	0.78343	0.19147
Mo	0.41297	0.54608	0.22304	-0.51437	-0.78343	0.80853
S	0.62083	0.87260	0.25530	-0.21270	-0.41750	0.94820
S	0.37917	0.12740	0.74470	-0.78730	0.41750	0.05180
S	0.25530	0.62083	0.87260	-0.26930	-0.41800	0.47220
S	0.74470	0.37917	0.12740	-0.73070	0.41800	0.52780
S	0.87260	0.25530	0.62083	-0.79460	0.92020	0.06350
S	0.12740	0.74470	0.37917	-0.20540	-0.92020	0.93650
S	0.78627	0.78627	0.78627	-0.71490	-0.08660	0.53200
S	0.21373	0.21373	0.21373	-0.28510	0.08660	0.46800

TABLE IV: Information of the crystal structures of EuMo_6S_8 in the $R\bar{3}$ phase (ICDD PDF: 00-048-1791) [7] and the $P\bar{1}$ phase (ICDD PDF: 01-079-0877) [8].

	EuMo ₆ S ₈					
	$R\bar{3}$			$P\bar{1}$		
Lattice vectors (Å)						
a	4.58870	2.64929	3.85410	-0.08492	-0.08293	-6.59193
b	-4.58870	2.64929	3.85410	-0.21025	-6.56263	0.00000
c	0.00000	-5.29857	3.85410	-6.48200	0.00000	0.00000
Atom positions (fraction)						
Eu	0.00000	0.00000	0.00000	0.00000	0.00000	0.00000
Mo	0.43803	0.77274	0.58377	-0.43890	-0.58160	-0.76700
Mo	0.56197	0.22726	0.41623	-0.56110	-0.41840	-0.23300
Mo	0.22726	0.41623	0.56197	-0.76950	-0.44380	-0.58360
Mo	0.58377	0.43803	0.77274	-0.23050	-0.55620	-0.41640
Mo	0.41623	0.56197	0.22726	-0.58550	-0.78070	-0.43850
Mo	0.77274	0.58377	0.43803	-0.41450	-0.21930	-0.56150
S	0.87471	0.25789	0.61699	-0.60200	-0.23600	-0.85400
S	0.12529	0.74211	0.38301	-0.39800	-0.76400	-0.14600
S	0.74211	0.38301	0.12529	-0.75400	-0.76500	-0.75200
S	0.61699	0.87471	0.25789	-0.24600	-0.23500	-0.24800
S	0.38301	0.12529	0.74211	-0.26200	-0.84700	-0.62000
S	0.25789	0.61699	0.87471	-0.73800	-0.15300	-0.38000
S	0.75637	0.75637	0.75637	-0.88900	-0.62300	-0.26000
S	0.24363	0.24363	0.24363	-0.11100	-0.37700	-0.74000

-
- [1] J. D. Jorgensen and D. G. Hinks, Rhombohedral-to-triclinic phase transition in BaMo_6S_8 , *Physica B+C* **136**, 485 (1986), neutron Scattering.
- [2] W. Kalsbach, *Strukturelle Phasenübergänge und druckinduzierte Supraleitung von Molybdän-Clusterverbindungen (Chevrel-Phasen)*, Tech. Rep. Juel-1921 (Jülich, 1984).
- [3] B. Koppelhuber-Bitschnau, F. A. Mautner, and K. Yvon, Low-temperature structural phase transition in SrMo_6S_8 studied by x-ray powder diffraction, *Monatsh. Chem.* **121**, 505 (1990).
- [4] Mo_6S_8 (Mo_3S_4 rhom) crystal structure: Datasheet from “pauling file multinationals edition – 2012” in [springer materials](https://materials.springer.com/isp/crystallographic/docs/sd_0312550) (https://materials.springer.com/isp/crystallographic/docs/sd_0312550), copyright 2016 Springer-Verlag Berlin Heidelberg & Material Phases Data System (MPDS), Switzerland & National Institute for Materials Science (NIMS), Japan.
- [5] W. R. McKinnon and J. R. Dahn, Structure and electrochemistry of $\text{Li}_x\text{Mo}_6\text{S}_8$, *Phys. Rev. B* **31**, 3084 (1985).
- [6] H. Fukuoka, K. Masuoka, T. Hanaoka, and K. Inumaru, New polymorph of Mo_3S_4 prepared using a high-pressure synthesis technique: Crystal structure, electronic property, and band calculation, *Inorg. Chem.* **52**, 7918 (2013).

- [7] Ø. Fischer, A. Treyvaud, R. Chevrel, and M. Sargent, Superconductivity in the $\text{Re}_x\text{Mo}_6\text{S}_8$, *Solid State Commun.* **17**, 721 (1975).
- [8] S. Quezel, P. Burlet, A. Dinia, J. Rossat-Mignod, R. Horyn, O. Pena, and M. Sargent, Neutron diffraction study of the crystal and magnetic structures of $^{153}\text{EuMo}_6\text{S}_8$, *Phys. B: Condens. Matter* **156-157**, 780 (1989).